

Ten-moment fluid modeling of the Weibel instability

D.A. Kuldinow¹ and K. Hara¹

Plasma Dynamics Modeling Laboratory, Department of Aeronautics and Astronautics, Stanford
University, 496 Lomita Mall, Stanford, CA 94305, USA

Corresponding author: Derek Kuldinow, kuldinow@stanford.edu

(Received 1 December 2024; revision received 5 March 2025; accepted 6 March 2025)

We investigate the one-dimensional non-relativistic Weibel instability through the capture of anisotropic pressure tensor dynamics using an implicit 10-moment fluid model that employs the electromagnetic Darwin approximation. The results obtained from the 10-moment model are compared with an implicit particle-in-cell simulation. The linear growth rates obtained from the numerical simulations are in good agreement with the theoretical fluid and kinetic dispersion relations. The fluid dispersion relations are derived using Maxwell's equations and the Darwin approximation. We also show that the magnetohydrodynamic approximation can be used to model the Weibel instability if one accounts for an anisotropic pressure tensor and unsteady terms in the generalised Ohm's law. In addition, we develop a preliminary theory for the saturation magnetic field strength of the Weibel instability, showing good agreement with the numerical results.

Keywords: astrophysical plasmas, plasma simulation, plasma instabilities

1. Introduction

Plasmas with anisotropic velocity distribution functions (VDFs) are common both in astrophysical and laboratory plasmas when the collisional time scale is long compared with the dynamical time scales. Within magnetised plasmas, modified transport across magnetic field lines often results in different temperatures parallel and perpendicular to the magnetic field (Krall, Trivelpiece & Gross 1973). Even in the absence of strong magnetic fields, velocity space anisotropy can arise from interacting beams, shocks and radiative effects. The ultimate equilibrium state is isotropic, which can be achieved through intraspecies Coulomb collisions. However, collective effects like instabilities can often be more effective at driving the system towards equilibrium in regions of low collisionality.

The Weibel instability (Weibel 1959) is an electromagnetic plasma instability arising from anisotropy in velocity space. It has attracted attention in recent years due to its implications for the dynamics within astrophysical shocks (Nishikawa *et al.* 2003, 2006; Huntington *et al.* 2015), potentially generating strong magnetic fields to accelerate cosmic rays, and within laser-produced fusion-capable laboratory plasmas (Tatarakis *et al.* 2003; Ren *et al.* 2004; Mondal *et al.* 2012; Fiúza *et al.* 2012; Zhang *et al.* 2020).

Previous work has studied the evolution and saturation of the Weibel instability in detail through grid-based direct kinetic (Califano *et al.* 1998; Cagas *et al.* 2017a,b; Ghizzo, Sarrat & Del Sarto 2017) and particle-in-cell (PIC) simulations (Morse & Nielson 1970; Okada & Ogawa 2007; Chen & Chacón, 2014; Kaang, Ryu & Yoon 2009). Simulations in multiple spatial dimensions demonstrate how oblique propagating modes can cause damping and equipartition of energy in an electromagnetic plasma (Morse & Nielson 1970; Romanov *et al.* 2004; Ruyer *et al.* 2015). Certain laboratory and astrophysical plasmas also have a background equilibrium magnetic field; studies have found that such a field can affect the saturation amplitude of the Weibel instability, by trapping particles and modifying transport (Ji-Wei & Wen-Bing 2005; Stockem *et al.* 2007, 2008; Grassi *et al.* 2017).

Early work by Bychenkov, Silin & Tikhonchuk (1989) and Basu (2002) developed a fluid approach to studying the Weibel instability by retaining full pressure tensor dynamics. As opposed to an anisotropic temperature, the first numerical studies in the fluid regime considered two distinct cold populations, i.e. transverse two-stream and current filamentation instabilities (Pegoraro *et al.* 1996; Califano, Pegoraro & Bulanov 1997). The fluid model was then expanded to a full three-dimensional model, which demonstrated how the fluid approach couples the Weibel instability to two-stream and current-filamentation instabilities, predicting the thermal oblique propagating modes (Sarrat *et al.* 2016, 2017). However, there has been little study into implementing a computational warm plasma fluid model and comparing the linear growth and saturation dynamics with the kinetic model.

In this paper, we derive equivalent dispersion relations for the Weibel instability from various electromagnetic 10-moment fluid frameworks, including Maxwell's equations and the Darwin approximation, which are compared with the kinetic dispersion relation. Furthermore, we develop an implicit 10-moment numerical fluid model under the non-relativistic electromagnetic Darwin approximation and compare the 10-moment simulation results to PIC simulations and the fluid and kinetic theories. This paper is structured as follows. In §2, we present derivations of the dispersion relation for the one-dimensional Weibel instability from kinetic and fluid perspectives. In §3, we compare the growth rates obtained from the kinetic and fluid models for the electron and ion Weibel instabilities. In §4, we present a brief discussion on the saturation of the Weibel instability. In §5, we describe our numerical methods for the fluid and kinetic models. Finally, in §6, we present numerical results for the electron Weibel instability.

2. Linear dispersion theory of the Weibel instability

To study the electromagnetic Weibel instability, we perform linear analyses of the instability from kinetic and 10-moment (full pressure tensor) fluid perspectives.

2.1. Kinetic theory

The Weibel instability arises from initially considering a Maxwellian plasma with anisotropic temperatures, wherein the initial equilibrium plasma VDF is assumed to be of the form

$$f_{s,0} = \left(\frac{m_s}{2\pi k_B} \right)^{3/2} \frac{1}{\sqrt{T_{s,\parallel} T_{s,\perp}^2}} \exp \left[-\frac{m_s v_x^2}{2k_B T_{s,\parallel}} - \frac{m_s (v_y^2 + v_z^2)}{2k_B T_{s,\perp}} \right], \quad (2.1)$$

where m_s is the mass of species s , k_B is the Boltzmann constant, v_i is the species velocity in the i th direction, i.e. $i = \{1, 2, 3\} = \{x, y, z\}$, and we have assumed, without loss of generality, that the plasma species has temperature $T_{s,\parallel} = T_{s,x}$ in the x (\parallel) direction, different from the temperature $T_{s,\perp}$, where \perp refers to the directions perpendicular to x (i.e. y and z), and that we are in the reference frame where the species is at rest (i.e. there is no bulk velocity).

The electromagnetic perturbation analysis of this distribution function is presented in the literature (Weibel 1959) and textbooks (Krall *et al.* 1973), and is reproduced here for completeness. The dispersion relation is found by finding the zeros of the dielectric function (Krall *et al.* 1973) for perturbations in the x direction:

$$\begin{aligned} D_K(k_x, \omega) &= 1 - \frac{k_x^2 c^2}{\omega^2} - \sum_s \frac{\omega_{s,p}^2}{\omega^2} \left[1 + \int \frac{v_\perp^2 (\partial f_{s,0} / \partial v_x)}{v_x - \omega/k_x} d\mathbf{v} \right] \\ &= 1 - \frac{k_x^2 c^2}{\omega^2} - \sum_s \frac{\omega_{s,p}^2}{\omega^2} \left[1 + \frac{T_{s,\perp}}{2T_{s,\parallel}} Z'(\xi_s) \right] = 0, \end{aligned} \quad (2.2)$$

where $\omega_{s,p} = \sqrt{n_s e^2 / (m_s \epsilon_0)}$ is the species plasma frequency, where n_s is the species number density, e is the fundamental charge and ϵ_0 is the permittivity of free space, $\xi_s = \omega / (k_x \sqrt{2T_{s,\parallel} / m_s})$, and $Z'(\xi)$ is the first derivative of the plasma dispersion function (Fried & Conte 2015). Note that ξ may be interpreted as the wave speed normalised by the thermal velocity; or, in the case for imaginary ω , a normalised growth rate. It is oftentimes useful to employ the following asymptotic expansions for $Z'(\xi)$:

$$Z'(\xi) \simeq \begin{cases} -2i\sqrt{\pi}\xi e^{-\xi^2} + \frac{1}{\xi^2} + \frac{3}{2\xi^4} + \frac{15}{4\xi^6} + \dots & \text{for } |\xi| \gg 1, \\ -2i\sqrt{\pi}\xi e^{-\xi^2} - 2 + 4\xi^2 - \frac{8\xi^4}{3} + \dots & \text{for } |\xi| \ll 1. \end{cases} \quad (2.3)$$

2.2. Ten-moment fluid – Maxwell theory

To determine the fluid dispersion relation, we begin with the collisionless 10-moment fluid equations for a charged fluid using the primitive variables (Hakim 2008; Kuldinow *et al.* 2024b):

$$\frac{d\rho}{dt} + \rho \frac{\partial u_i}{\partial x_i} = 0, \quad (2.4)$$

$$\frac{du_i}{dt} + \frac{1}{\rho} \frac{\partial p_{ij}}{\partial x_j} = \frac{q}{m} (E_i + \epsilon_{ijk} u_j B_k), \quad (2.5)$$

$$\frac{dp_{ij}}{dt} + p_{ij} \frac{\partial u_k}{\partial x_k} + p_{jk} \frac{\partial u_i}{\partial x_k} + p_{ki} \frac{\partial u_j}{\partial x_k} + \frac{\partial q_{ijk}}{\partial x_k} = \frac{q}{m} (\epsilon_{ikm} p_{jk} B_m + \epsilon_{jkm} p_{ik} B_m), \quad (2.6)$$

where $\frac{d}{dt} = \frac{\partial}{\partial t} + u_i \frac{\partial}{\partial x_i}$ is the Lagrangian derivative, ρ is the species mass density, u_i is the species bulk velocity, p_{ij} is the species pressure tensor, q_{ijk} is the species heat flux tensor, E_i and B_i are the electric and magnetic fields, respectively, the species has charge q and mass m , and ϵ_{ijk} is the Levi–Civita symbol, employing the Einstein summation convention.

Note that conventional 5-moment models, which solve for ρ , u_i and a total energy \mathcal{E} , require closure for the isotropic pressure, p , and deviatoric stress tensor, τ_{ij} . The pressure is usually closed by the equation of state, which is usually described using a polytropic index, and the stress tensor is typically described using a constitutive model (e.g. viscosity and shear). However, the 10-moment model explicitly formulates the pressure tensor evolution, which eliminates the use of an equation of state for the pressure and now only requires closure in the heat flux (third velocity moment).

For the derivation of a Weibel-type instability, we will assume a one-dimensional slab geometry in the x direction, i.e. $\partial_y = \partial_z = 0$, and we will only need equations for u_y and p_{xy} , which will lead to only to field components B_z and E_y . It is to be noted that perturbations to the density, ρ , longitudinal velocity, u_x , and diagonal pressure elements, $\{p_{xx}, p_{yy}, p_{zz}\}$, only couple to the growth of the Weibel instability through second-order terms. For linear perturbations, only the transport equations for u_y and p_{xy} need to be considered, which can be written from (2.5) and (2.6) as

$$\frac{du_y}{dt} + \frac{1}{\rho} \frac{\partial p_{xy}}{\partial x} = \frac{q}{m} (E_y + u_z B_x - u_x B_z), \quad (2.7)$$

$$\frac{dp_{xy}}{dt} + 2p_{xy} \frac{\partial u_x}{\partial x} + p_{xx} \frac{\partial u_y}{\partial x} + \frac{\partial q_{xxy}}{\partial x} = \frac{q}{m} [p_{xz} B_x + (p_{yy} - p_{xx}) B_z - p_{yz} B_y]. \quad (2.8)$$

These equations must now be coupled with the Maxwell equations for the evolution of the electric and magnetic fields. In particular, we take linear perturbations of Faraday's law and Ampère's law for the magnetic field in only the z direction:

$$\frac{\partial B_z}{\partial t} = -\frac{\partial E_y}{\partial x}, \quad (2.9)$$

$$-\frac{\partial B_z}{\partial x} = \mu_0 \sum_s \frac{q_s \rho_s}{m_s} u_{s,y} + \mu_0 \epsilon_0 \frac{\partial E_y}{\partial t}, \quad (2.10)$$

where μ_0 is the vacuum permeability. Now, we may take perturbations around an initially uniform, stationary, field-less, but anisotropic initial condition:

$$\rho = \rho_0 + \rho' \varpi, \quad u_i = u'_i \varpi, \quad (2.11)$$

$$p_{xx} = p_{xx,0} + p'_{xx} \varpi, \quad p_{yy} = p_{yy,0} + p'_{yy} \varpi, \quad p_{zz} = p_{zz,0} + p'_{zz} \varpi, \quad (2.12)$$

$$p_{xy} = p'_{xy} \varpi, \quad p_{xz} = p'_{xz} \varpi, \quad p_{yz} = p'_{yz} \varpi, \quad (2.13)$$

$$q_{xxy} = 0, \quad E_i = E'_i \varpi, \quad B_i = B'_i \varpi, \quad (2.14)$$

where quantities subscripted with 0 are invariant in space, primed quantities are assumed small and the linear perturbations are assumed as $\varpi = \exp[i(k_x x - \omega t)]$. The assumption that $q_{xxy} = 0$ is justified by comparing with the theory presented by Kuldinow *et al.* (2024b), where $q_{xxy} \propto \partial_y T$. Since we are assuming no variation in the y direction, the estimate for the fluid heat flux vanishes. Note that this argument is independent of whether we are in the linear or nonlinear regime. For collisionless plasmas, spectral or non-local heat flux models, like those developed by Hammett &

Perkins (1990) and Sharma *et al.* (2006), may provide better agreement with kinetic results. The magnetic field suppresses cross-field transport (Mitchner & Kruger Jr. 1973), also limiting the importance of heat flux. However, studying the effect of heat flux closures on the behaviour of the fluid Weibel instability is reserved for future work.

Substituting these forms of the variables into (2.7)–(2.10) and keeping only terms to first order, we obtain

$$-i\omega u'_y + \frac{ik_x p'_{xy}}{\rho_0} = \frac{q}{m} E'_y, \quad (2.15)$$

$$-i\omega p'_{xy} + ik_x p_{xx,0} u'_y = \frac{q B'_z}{m} (p_{yy,0} - p_{xx,0}), \quad (2.16)$$

$$-i\omega B'_z = -ik_x E'_y, \quad (2.17)$$

$$-ik_x B'_z = \mu_0 \epsilon_0 \sum_s \frac{q_s \rho_{s,0}}{m_s \epsilon_0} u'_{s,y} - i\mu_0 \epsilon_0 \omega E'_y. \quad (2.18)$$

Algebraic manipulations yield the following dispersion relation for the 10-moment Maxwell Weibel instability:

$$D_{10M}(k_x, \omega) = 1 - \frac{k_x^2 c^2}{\omega^2} - \sum_s \frac{w_{s,p}^2}{\omega^2} \left(1 + \frac{T_{s,\perp}}{2T_{s,\parallel}} \frac{1}{\xi_s^2 - 1/2} \right) = 0. \quad (2.19)$$

Equation (2.19) is consistent with previous work (Sarrat *et al.* 2016, 2017) and care has been taken to express the dielectric function in a form reminiscent of the kinetic dispersion relation. By comparing with the kinetic dispersion relation, i.e. (2.2), we observe that for large ξ , $D_K(k_x, \omega) = D_{10M}(k_x, \omega) + O(\xi^{-4})$. Recalling that ξ is a normalised wavespeed, this indicates good agreement between the two models at large values of $\omega/k_x \propto \xi$. It is discussed later that $\text{Re}(\omega) \approx 0 \ll \text{Im}(\omega)$ for the Weibel instability, so large values of ω correspond to large Weibel growth rates.

2.3. Ten-moment fluid – Darwin approximation

In the Darwin approximation, the plasma is assumed to be non-relativistic, that is, the bulk velocity in (2.10) obeys $u \ll c$, and also that the thermal speed $\sqrt{k_B T/m} \ll c$. Thus, the displacement current is negligible in the frequencies of interest ($\omega \ll ck_x$). The Darwin equations are written in terms of the electric scalar potential, ϕ , and the magnetic vector potential, A_i , as

$$\frac{\partial^2 \phi}{\partial x_k \partial x_k} = - \sum_s \frac{q_s \rho_s}{m_s \epsilon_0}, \quad (2.20)$$

$$\frac{\partial^2 A_i}{\partial x_k \partial x_k} = \mu_0 \epsilon_0 \frac{\partial^2 \phi}{\partial t \partial x_i} - \sum_s \frac{\mu_0 q_s \rho_s u_{s,i}}{m_s}, \quad (2.21)$$

from which the electric and magnetic fields are found as

$$E_i = -\frac{\partial \phi}{\partial x_i} - \frac{\partial A_i}{\partial t}, \quad B_i = \epsilon_{ijk} \frac{\partial A_k}{\partial x_j}. \quad (2.22)$$

In one spatial dimension, (2.20) and (2.21) reduce to

$$\frac{\partial^2 \phi}{\partial x^2} = - \sum_s \frac{q_s \rho_s}{m_s \epsilon_0}, \quad (2.23)$$

$$\frac{\partial^2 A_{\perp}}{\partial x^2} = - \sum_s \frac{\mu_0 q_s \rho_s u_{s,\perp}}{m_s}. \quad (2.24)$$

As the perturbations of ρ are second-order effects, the perturbations of ϕ are also second order from (2.23). Similar to Maxwell's equations, we only need the perturbations of E_y and B_z for the linear perturbation analysis. The linear perturbations of (2.22) and (2.24) yield

$$E'_y = i\omega A'_y = \frac{\omega}{k_x} (ik_x A'_y) = \frac{\omega}{k_x} B'_z \quad (2.25)$$

and

$$B'_z = ik_x A'_y = \frac{i\mu_0 \epsilon_0}{k_x} \sum_s \frac{q_s \rho_{s,0}}{m_s \epsilon_0} u'_{s,y}, \quad (2.26)$$

respectively. By comparison to the Maxwell system in the previous section, (2.25) and (2.17) are identical, while (2.26) is equivalent to (2.18) but sans the displacement current term. Substituting the Darwin model ((2.25) and (2.26)) into the 10-moment fluid equations ((2.15) and (2.16)), we obtain the dispersion relation for the 10-moment Darwin Weibel instability:

$$D_{10D}(k_x, \omega) = -\frac{k_x^2 c^2}{\omega^2} - \sum_s \frac{w_{s,p}^2}{\omega^2} \left(1 + \frac{T_{s,\perp}}{2T_{s,\parallel}} \frac{1}{\xi_s^2 - 1/2} \right) = 0. \quad (2.27)$$

It is to be noted that the first term on the right-hand side of (2.19) is eliminated using the Darwin approximation in (2.27) under the assumption that $k_x^2 c^2 / \omega^2 \gg 1$.

2.4. Magnetohydrodynamic approximation

Another common assumption in the plasmadynamics community is the magnetohydrodynamic (MHD) approximation. The plasma is considered as a single fluid, rather than a sum of individual fluids. The equations are then written in terms of the total mass density, $\bar{\rho}$, mass velocity, U_i , and net current density, j_i :

$$\bar{\rho} = \sum_s \rho_s = \bar{n} \sum_s m_s, \quad (2.28)$$

$$U_i = \frac{1}{\bar{\rho}} \sum_s \rho_s u_{s,i}, \quad (2.29)$$

$$j_i = \sum_s \frac{q_s \rho_s u_{s,i}}{m_s}. \quad (2.30)$$

The MHD equations of motion are derived by summing or differencing the individual fluid species equations of motion to obtain equations for the bulk plasma

quantities $\{\bar{\rho}, U_i, j_i\}$. The field dynamics are modified to use Ampère's equation (neglecting the displacement current) and the generalised Ohm's law, which is equivalent to the fluid momentum equations, assuming that $m_e/m_i \ll 1$ and $T_i \lesssim T_e$, where e and i refer to electron and ion species, respectively. The evolution and field equations in MHD are written (Krall *et al.* 1973)

$$\frac{\partial \bar{\rho}}{\partial t} + U_i \frac{\partial \bar{\rho}}{\partial x_i} + \bar{\rho} \frac{\partial U_i}{\partial x_i} = 0, \quad (2.31)$$

$$\bar{\rho} \frac{\partial U_i}{\partial t} + U_j \frac{\partial U_i}{\partial x_j} = \epsilon_{ijk} j_j B_k - \frac{\partial p_{e,ij}}{\partial x_j}, \quad (2.32)$$

$$E_i + \epsilon_{ijk} U_j B_k = -\frac{1}{e\bar{n}} \frac{\partial p_{e,ij}}{\partial x_j} + \frac{m_e}{\bar{n}e^2} \frac{dj_i}{dt}, \quad (2.33)$$

$$\epsilon_{ijk} \frac{\partial B_k}{\partial x_j} = \mu_0 j_i, \quad (2.34)$$

where the final term in (2.33), i.e. the unsteady component in Ohm's law, provides feedback from the magnetic field to the currents and is important in recovering the correct Weibel instability dynamics. The electron inertia terms ($\propto u \partial_x u$) are negligible for the linear perturbation theory assuming an initially stationary electron fluid, i.e. $\vec{u}_{e,0} = 0$. The generalised Ohm's law in (2.33) can be inserted into Faraday's equation to obtain

$$\frac{\partial B_i}{\partial t} = \epsilon_{ijk} \frac{\partial}{\partial x_j} \left(\epsilon_{klm} U_l B_m + \frac{1}{e\bar{n}} \frac{\partial p_{e,kl}}{\partial x_l} - \frac{m_e}{\bar{n}e^2} \frac{\partial j_k}{\partial t} \right). \quad (2.35)$$

This conclusion is similar in form to previous work discussing the role of the so-called 'canonical battery effect' in magnetic reconnection (Yoon & Bellan 2019) and magnetogenesis (Laishram, Yun & Yoon 2024).

Taking perturbations of (2.31)–(2.35) and coupling them to the pressure evolution equation, (2.16), yields the linear dispersion relation for the 10-moment MHD Weibel instability:

$$D_{10\text{MHD}}(k_x, \omega) = -\frac{k_x^2 c^2}{\omega^2} - \frac{\omega_{e,p}^2}{\omega^2} \left(1 + \frac{T_{e,\perp}}{2T_{e,\parallel}} \frac{1}{\xi_e^2 - 1/2} \right) = 0. \quad (2.36)$$

Here, it can be seen that (2.36) is consistent with (2.27) when only accounting for the electron susceptibility, $s = e$. Without the unsteady component to Ohm's law, the parenthetical term in (2.36) becomes $1 - T_{\perp}/T_{\parallel} - 2\xi^2$, which is inconsistent with the kinetic solution for all ξ . Including the unsteady component, however, achieves an equivalent dispersion relation to the 10-moment model with Darwin equations. Thus, to accurately capture the Weibel instability using the MHD approximation, the unsteady component must be retained in the generalised Ohm's law. Furthermore, our theory suggests that for extended MHD-type simulations, including a full pressure tensor but not retaining the unsteady component to Ohm's law may lead to unphysical instability growth from the incorrect dispersion relation. A full derivation and discussion of (2.36) is presented in Appendix A.

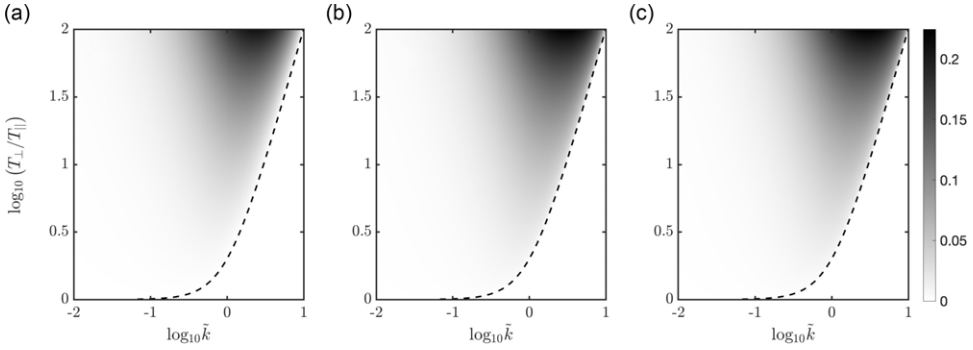


FIGURE 1. Theoretical growth rates, $\tilde{\gamma} = \gamma/\omega_{e,p}$ for the electron Weibel instability with $\tilde{T}_{e,\parallel} = 6.25 \times 10^{-4}$, showing the cutoff wavenumber (dashed line) and using the (a) kinetic dispersion relation, (2.2), (b) 10-moment Maxwell dispersion relation, (2.19), and (c) 10-moment Darwin dispersion relation, (2.27).

3. Comparison of kinetic and fluid dispersion relations

We present normalised results, where each quantity is normalised by a reference value

$$\begin{aligned} \tilde{\omega} &= \frac{\omega}{\omega_{e,p}}, & \tilde{k}_x &= \frac{k_x c}{\omega_{e,p}}, & \tilde{m} &= \frac{m}{m_e}, & \tilde{q} &= \frac{q}{e}, & \tilde{E} &= \frac{eE}{m_e c \omega_{e,p}}, & \tilde{B} &= \frac{eB}{m_e \omega_{e,p}}, \\ \tilde{n} &= \frac{ne^2}{m_e \epsilon_0 \omega_{e,p}^2}, & \tilde{u} &= \frac{u}{c}, & \tilde{T}_s &= \frac{2k_B T_s}{m_s c^2}, & \tilde{\xi}_s &= \frac{\tilde{\omega}}{\tilde{k} \sqrt{\tilde{T}_{s,\parallel}/\tilde{m}_s}}. \end{aligned} \quad (3.1)$$

The kinetic dispersion relation, (2.2), is solved by evaluating $Z(\xi) = i\sqrt{\pi}w(\xi)$, where $w(\xi)$ is the Faddeeva function, which is numerically calculated using the methods of Gautschi (1970) and Zaghloul & Ali (2012). The fluid dispersion relations, i.e. the 10-moment Maxwell and 10-moment Darwin models, are solved analytically by inverting the degree-four polynomials in (2.19) and (2.27), respectively.

3.1. Electron Weibel growth rate

Figure 1 shows the electron Weibel growth rate, i.e. $\tilde{\gamma} = \text{Im}(\tilde{\omega})$, as a function of \tilde{k}_x and $T_{e,\perp}/T_{e,\parallel}$ for $\tilde{T}_{e,\parallel} = 6.25 \times 10^{-4}$ or $\sqrt{\tilde{T}_{e,\parallel}/\tilde{m}_e} = 0.025$ for $\tilde{k}_x \in [0.01, 10]$ and $T_{e,\perp}/T_{e,\parallel} \in [1, 100]$. Here, the ion susceptibility is neglected. There is negligible difference ($< 1\%$ for the entire plot) between the Maxwell and Darwin fluid growth rates for the parameters chosen, as shown in figures 1(b) and 1(c), respectively, since $\sqrt{\tilde{T}_{e,\parallel}/\tilde{m}_e} \ll \tilde{c} = 1$. While good qualitative agreement can be observed between all the models, the 10-moment fluid dispersion relations (figures 1(b,c)) predict slightly higher growth rates than the kinetic dispersion relation (figure 1(a)). It is to be noted that the real frequency $\omega_r = \text{Re}(\tilde{\omega}) \simeq 0$ in each of these plots, because (2.2), (2.19) and (2.27) are functions of ω^2 in the high- ξ limit and thus admit purely imaginary solutions.

For every wavenumber \tilde{k}_x , we note that there is a cutoff temperature ratio, T_{\perp}/T_{\parallel} , under which the instability does not grow. Or conversely, for a given temperature ratio, there is a maximum wavenumber above which there is no instability. The

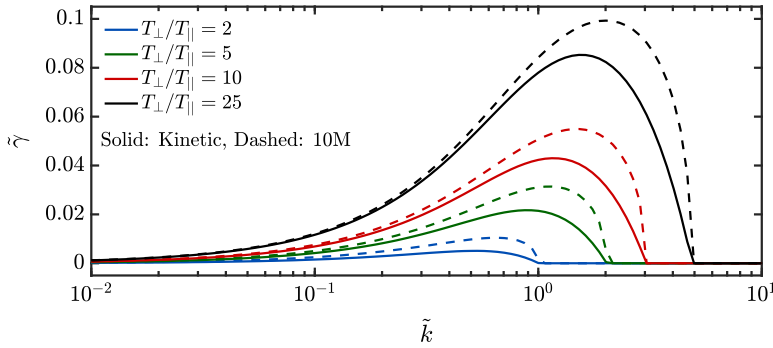


FIGURE 2. Plot of $\tilde{\gamma}_K$ (solid lines; kinetic) and $\tilde{\gamma}_F$ (dashed lines; 10-moment Darwin, which is almost identical to 10-moment Maxwell) for the electron Weibel instability as a function of the wavenumber for various values of the temperature ratio T_{\perp}/T_{\parallel} .

cutoff condition occurs when $\xi = 0$ solves the dispersion relation. Multiplying (2.2) by ω^2 and taking the limit of $\{\omega, \xi\} \rightarrow 0$, noting that $Z'(0) = -2$, since $Z'(\xi) = -2[1 + \xi Z(\xi)]$ (see also (2.3)), we find that the cutoff condition can be written as

$$(k_x)_{\text{cutoff}} = \sqrt{\sum_s \frac{\omega_{s,p}^2}{c^2} \left(\frac{T_{s,\perp}}{T_{s,\parallel}} - 1 \right)} = \frac{\omega_{e,p}}{c} \sqrt{\sum_s \frac{m_e}{m_s} \left(\frac{T_{s,\perp}}{T_{s,\parallel}} - 1 \right)}, \quad (3.2)$$

which describes the cutoff k_x for a given T_{\perp}/T_{\parallel} for each species. For the electron Weibel instability, we can also write the cutoff temperature ratio for a given k_x as

$$\left(\frac{T_{\perp}}{T_{\parallel}} \right)_{\text{cutoff}} = 1 + \left(\frac{k_x c}{\omega_p} \right)^2. \quad (3.3)$$

Furthermore, by performing a similar treatment to the above with the 10-moment dispersion relations, (2.19) and (2.27), one obtains the exact same cutoff condition as the kinetic result. The cutoff condition is plotted as a dotted line in figure 1.

In figure 2, we present plots of the kinetic and fluid growth rates for various choices of the temperature ratio to provide a quantitative comparison. For a particular k_x (e.g. $\tilde{k}_x < 0.3$), as the temperature ratio increases, the agreement between the kinetic and fluid predictions converge. This is due to the fact that the growth rate γ (and $\xi \propto \gamma$) increases with T_{\perp}/T_{\parallel} and thus the fluid dispersion relation more closely approximates the kinetic one. It can be seen from figure 2 that the cutoff condition occurs as predicted in (3.2).

We also note that the fluid models provide good order-of-magnitude estimates for the maximum growth rate and the wavenumber at which the growth rate is largest. Using the 10-moment Darwin (10D) theory (2.27) and solving for $d\omega/dk = 0$, we can analytically determine the wavenumber of the maximum growth rate, i.e. $(k_x)_{\text{max}}$, and the maximum growth rate, γ_{max} :

$$(k_x)_{\text{max},10D} = \frac{\omega_p}{c} \left(\sqrt{\frac{T_{\perp}}{T_{\parallel}}} - 1 \right)^{1/2}, \quad \gamma_{\text{max},10D} = \frac{\omega_p}{c} \sqrt{\frac{T_{\parallel}}{m}} \left(\sqrt{\frac{T_{\perp}}{T_{\parallel}}} - 1 \right). \quad (3.4)$$

To determine these values for the full kinetic dispersion relation, one would need to solve the plasma dispersion function, for which there is no closed-form solution.

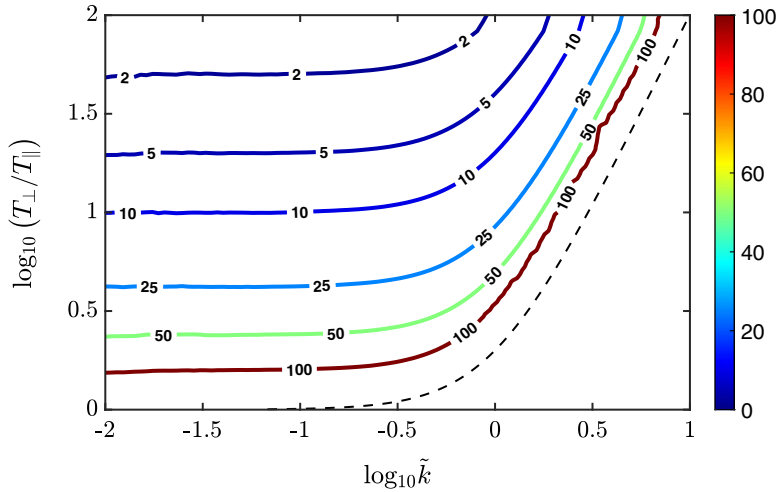


FIGURE 3. Relative discrepancy between kinetic and 10-moment Maxwell fluid growth rates $\Delta = |\gamma_F/\gamma_K - 1|(\%)$. The dashed line denotes the cutoff wavenumber.

To quantify the discrepancy between the kinetic and fluid dispersion relations, figure 3 presents the relative error of the linear growth rates between the fluid and kinetic theories. The relative error is defined as

$$\Delta = \left| \frac{\gamma_F - \gamma_K}{\gamma_K} \right| = \left| \frac{\gamma_F}{\gamma_K} - 1 \right|,$$

where γ_K is the growth rate calculated from the kinetic theory, (2.2), and γ_F is the growth rate calculated from the fluid theory, (2.19). The relative error is greatest near to the cutoff wavenumber, where both growth rates go to zero. However, the error decreases linearly with T_\perp/T_\parallel at large temperature ratios (e.g. $T_\perp/T_\parallel > 3$ and $\tilde{k}_x < 0.3$). By combining (2.27) and (3.3), we can estimate for the fluid dispersion relations for $T_\perp/T_\parallel \gg 1$:

$$\xi^2 = \frac{1}{2} \left[1 - \frac{T_\perp/T_\parallel}{(T_\perp/T_\parallel)_{\text{cutoff}}} \right] \simeq -\frac{1}{2} \frac{T_\perp/T_\parallel}{(T_\perp/T_\parallel)_{\text{cutoff}}}, \quad (3.5)$$

where $(T_\perp/T_\parallel)_{\text{cutoff}}$ is given in (3.3). Furthermore, we can relate the relative error in the growth rate between the kinetic and fluid dispersion relations to the relative error in the estimate of the dispersion function:

$$\left| \frac{\delta\gamma}{\gamma} \right| = \left| \frac{\delta\xi}{\xi} \right| \simeq \left| \frac{\delta Z'}{2Z'} \right|, \quad (3.6)$$

where the final equality is obtained by estimating $Z' \simeq 1/\xi^2$. By comparing the first two terms of the kinetic Z' (2.3) with the 10-moment Darwin dispersion relation (2.27), we find that

$$\left| \frac{\delta Z'}{Z'} \right| = \left| \frac{1}{Z'(\xi)} \left(Z'(\xi) - \frac{1}{\xi^2 - 1/2} \right) \right| \simeq \frac{1}{\xi^2}. \quad (3.7)$$

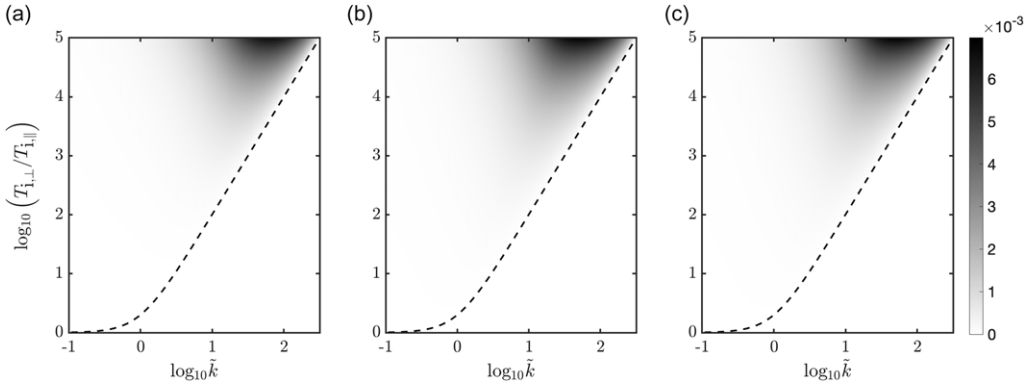


FIGURE 4. Theoretical growth rates, $\tilde{\gamma} = \gamma/\omega_{e,p}$, for the ion Weibel instability as a function of the ion temperature ratio and wavenumber. Here, $\tilde{T}_{e,\parallel} = \tilde{T}_{e,\perp} = 6.25 \times 10^{-4}$ and $\tilde{T}_{i,\parallel} = 1 \times 10^{-6}$. (a) Kinetic dispersion relation, (2.2). (b) Ten-moment Maxwell dispersion relation, (2.19). (c) Ten-moment Darwin dispersion relation, (2.27).

Substituting (3.5) into (3.6) and (3.7), we find that the relative error in the growth rate between the kinetic and fluid dispersion relations can be written as

$$\Delta \approx \frac{(T_{\perp}/T_{\parallel})_{\text{cutoff}}}{T_{\perp}/T_{\parallel}} \quad (3.8)$$

for large temperature ratios, $T_{\perp}/T_{\parallel} \gg 1$. It is for this reason that in figure 3, we see, for instance, an error of approximately 10 % for $T_{\perp}/T_{\parallel} = 10$ at small k_x away from the cutoff wavenumber, e.g. $k_x \leq (k_x)_{\text{cutoff}}/10$.

It is to be noted that, by combining (3.3), (3.4) and (3.8), the relative error in the growth rate estimate at the wavenumber of maximum growth can be obtained as

$$\Delta_{\text{max}} = \frac{1 + (k_{\text{max}} c/\omega_p)^2}{T_{\perp}/T_{\parallel}} = \left(\frac{T_{\perp}}{T_{\parallel}} \right)^{-1/2}. \quad (3.9)$$

3.2. Ion Weibel growth rate

The previous analysis considered hot electrons with anisotropic temperature and cold (immobile) ions, that is, ions do not participate in the dynamics or the growth rate. The ion Weibel instability arises when there is a strong temperature anisotropy in the ions, rather than electrons. Due to their heavy mass, ions often require longer times to suffer sufficient collisions to come to equilibrium and thus can often retain more anisotropy than electrons (Ng *et al.* 2020). Ion populations with different drift velocities can act as a large effective temperature anisotropy, leading to ion Weibel-like instabilities (Chang, Wong & Wu 1990).

Figure 4 shows the ion Weibel growth rate, i.e. $\tilde{\gamma} = \text{Im}(\tilde{\omega})$, as a function of \tilde{k}_x and $T_{i,\perp}/T_{i,\parallel}$; the cutoff condition as defined in (3.3) is plotted as a dotted line. We assume a hydrogen plasma (i.e. $m_i/m_e = 1836$) and set $T_{e,\parallel} = T_{e,\perp}$, so that the electron Weibel instability does not occur. Here, $\sqrt{\tilde{T}_{e,\parallel}/\tilde{m}_e} = \sqrt{\tilde{T}_{e,\perp}/\tilde{m}_e} = 0.025$ and $\sqrt{\tilde{T}_{i,\parallel}/\tilde{m}_i} = 0.001$ for $\tilde{k}_x \in [0.1, 300]$ and $T_{i,\perp}/T_{i,\parallel} \in [1, 10^5]$. This study includes

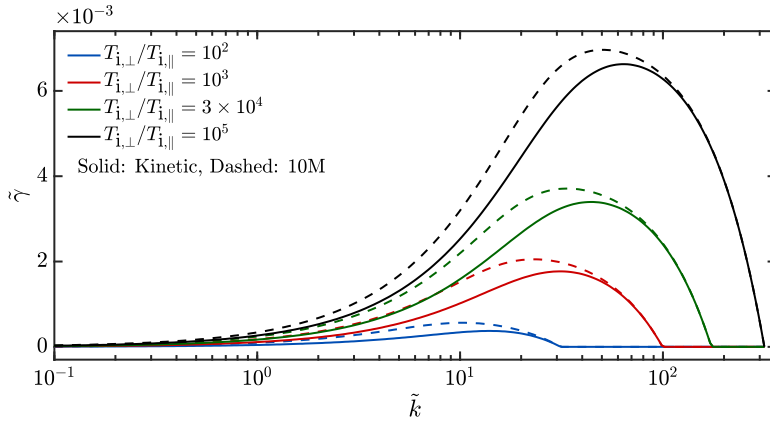


FIGURE 5. Plot of $\tilde{\gamma}_K$ (solid lines; kinetic) and $\tilde{\gamma}_F$ (dashed lines; 10-moment Darwin, which is almost identical to 10-moment Maxwell) for the ion Weibel instability as a function of the wavenumber for various values of the temperature ratio $T_{i,\perp}/T_{i,\parallel}$.

both warm electrons and ions where $T_{i,\parallel}/T_{e,\parallel} \approx 2.94$. We note that the ion Weibel growth rate (γ_{iW}) is much smaller than the electron Weibel growth rate (γ_{eW}); namely, $\gamma_{eW}/\omega_{e,p} = 0.1$ is achieved in the electron Weibel instability for electron temperature ratios of approximately $T_{e,\perp}/T_{e,\parallel} = 25$; however, $\gamma_{iW}/\omega_{i,p} = 0.1$ is achieved for ion temperature ratios $T_{i,\perp}/T_{i,\parallel} \gtrsim 10^4$. Similar to the electron Weibel instability, the discrepancy between the Maxwell and Darwin fluid growth rates is $< 1\%$ for the parameters chosen here, since the thermal speeds of each species are much less than the speed of light. The small value of γ also ensures that $(k_x c/\omega)^2 \gg 1$ and that the Darwin approximation is valid.

In figure 5, we present the kinetic and fluid growth rates for the various choices of the ion temperature ratio, $T_{i,\perp}/T_{i,\parallel}$, to provide a quantitative comparison. Note that the behaviour here is different from the electron Weibel instability in figure 2. Most notably, the fluid growth rates (dashed lines) do not converge to the kinetic growth rate (solid lines) as $T_{i,\perp}/T_{i,\parallel}$ increases for all k_x , while the cutoff condition obtained from the kinetic and 10-moment dispersion relations is identical, as explained in § 3.1. The discrepancy even at small k_x can be explained by noting that the kinetic dispersion relation reduces to the fluid theory only when both $\xi_e \gg 1$ and $\xi_i \gg 1$. For the electron Weibel instability, indeed $\xi_e \gg 1$, resulting in the convergence of kinetic and fluid theories at small \tilde{k}_x , as shown in figure 2. However, for the ion Weibel instability, the values of ξ are reduced compared with the electron Weibel instability because (1) $|\tilde{\gamma}| = |\tilde{\omega}| < 10^{-2}$ is small (note: $\omega_r = 0$) and (2) the growth rates are positive for higher \tilde{k}_x . These factors lead to $\xi_e \ll 1$, contributing to the discrepancies between the fluid and kinetic theories. Nonetheless, the fluid theories predict the correct cutoff condition, and we note qualitatively good agreement in the magnitude of the ion Weibel instability growth rate obtained from the 10-moment dispersion relation with the kinetic theory due to $\xi_i \gtrsim 1$.

4. Nonlinear saturation of the Weibel instability

Linear theories cannot directly predict saturation properties. However, the energy for the linear growth of the Weibel instability derives from the difference in parallel

and perpendicular temperatures. This state decays towards isotropic thermal equilibrium and in doing so, produces magnetic fields. Although the plasma is initially assumed to be an anisotropic Maxwellian, there is no reason to assume that a collisionless plasma will remain so after saturation of the Weibel instability. Thus, the analysis from a fluid standpoint, neglecting heat flux, provides an estimate of the saturation properties based on extending the behaviour of linear perturbations to saturation.

One could estimate that saturation occurs when the two temperatures p_{\parallel} , p_{\perp} equilibrate to one another. However, the perturbations to the diagonal pressure elements are second-order; thus, determining when the temperatures relax to one another would require second-order analysis. Still, a good heuristic for when saturation occurs can be obtained by considering only one warm species and studying the amplitude of the off-diagonal pressure element p_{xy} . Using (2.15)–(2.18), and substituting $\omega = i\gamma$ since $\omega_r = 0$, we find that

$$B'_z = \frac{p'_{xy}}{p_{\perp,0}} \frac{\gamma m}{q} \left(1 + \frac{k_x^2}{\gamma^2} \frac{p_{\parallel,0}}{\rho_0} \right). \quad (4.1)$$

Approximating that $\max(p'_{xy}) \simeq p_{\perp,0} - p_{\parallel,0}$, the average magnetic field energy density for a sinusoidal perturbation with wavenumber k_x can be written as

$$\left\langle \frac{B^2}{2\mu_0} \right\rangle = \frac{k_x}{2\pi} \int_0^{2\pi/k_x} \frac{1}{2\mu_0} B_z^2 dx = \frac{\rho_0 c^2 \gamma^2}{4 \omega_p^2} \left[\left(1 - \frac{T_{\parallel,0}}{T_{\perp,0}} \right) \left(1 + \frac{k_x^2}{\gamma^2} \frac{p_{\parallel,0}}{\rho_0} \right) \right]^2. \quad (4.2)$$

In the limit of large temperature ratios (i.e. $T_{\perp}/T_{\parallel} \gg 1$), where the fluid approximation is most valid, we can analytically solve (2.27) to obtain that

$$\gamma^2 \simeq \frac{p_{\perp,0} - p_{\parallel,0}}{\rho_0} \frac{\omega_p^2}{c^2 + \omega_p^2/k_x^2}. \quad (4.3)$$

Then, substituting (4.3) into (4.2) and taking $T_{\perp}/T_{\parallel} \rightarrow \infty$,

$$\left\langle \frac{B^2}{2\mu_0} \right\rangle \simeq \frac{p_{\perp,0} - p_{\parallel,0}}{4} \frac{1}{1 + \omega_p^2/c^2 k_x^2}. \quad (4.4)$$

This analysis has been for a known perturbation wavenumber k_x . However, for large enough system sizes, the wavenumber of maximum growth will be excited so we can directly substitute the formulae in (3.4) into (4.2), doing so yields an estimate for the maximum magnetic field saturation amplitude:

$$\left\langle \frac{B^2}{2\mu_0} \right\rangle_{\max} \simeq \frac{p_{\perp,0}}{4} \left(1 - \frac{T_{\parallel,0}}{T_{\perp,0}} \right)^2. \quad (4.5)$$

This relation implies that the maximum energy (density) extractable from a pressure difference is approximately one-quarter of the transverse pressure.

5. Numerical methods

To demonstrate the ability of 10-moment fluid models to capture the Weibel instability, we present kinetic (i.e. PIC) and fluid (i.e. 10-moment) simulations for the

electron Weibel instability. As noted in previous work (Nielson & Lewis 1976), due to its elliptic nature, the Darwin system is unconditionally unstable for explicit time integration and $k_{\min} \gtrsim \omega_{e,p}/c$, i.e. $L_x \gtrsim c/\omega_{e,p}$. Since this can be a strong limit on the maximum domain size, we employ implicit models in both the kinetic and fluid settings.

5.1. Kinetic model

We use an implicit charge-, canonical momentum- and energy-conserving Darwin electromagnetic particle-in-cell (EM-PIC) model, described by Chen & Chacón (2014). The model has been tested against Weibel instability theory and other standard electromagnetic test cases.

The EM-PIC model employs a Crank–Nicolson discretisation for the particle update:

$$\frac{x_p^{v+1} - x_p^v}{\Delta \tau^v} = v_{p,x}^{v+\frac{1}{2}}, \quad (5.1)$$

$$\frac{v_{p,i}^{v+1} - v_{p,i}^v}{\Delta \tau^v} = \frac{q_p}{m_p} \left(E_{p,i}^{v+\frac{1}{2}} + \epsilon_{ijk} v_{p,j}^{v+\frac{1}{2}} B_{p,k}^{v+\frac{1}{2}} \right), \quad (5.2)$$

where $\{x_p, v_{p,i}\}$ is the particle position and velocity, $\Delta \tau^v$ is the v th substep within Δt , $E_{i,p}^{v+\frac{1}{2}} = E_i \left(x_p^{v+\frac{1}{2}}, t^{v+\frac{1}{2}} \right)$ and $B_{i,p}^{v+\frac{1}{2}} = B_i \left(x_p^{v+\frac{1}{2}}, t^{v+\frac{1}{2}} \right)$ are the electric and magnetic fields interpolated to the particle position at the half-substep time, and following a Crank–Nicolson-type discretisation, $X^{v+\frac{1}{2}} = (X^{v+1} + X^v)/2$ for all quantities X . The particle velocity is updated using the Boris method. Note that both the particle positions and velocities are defined on the full-substep times, and the velocity update, (5.2), requires the fields at $x^{v+\frac{1}{2}}$, which itself is dependent on $v^{v+\frac{1}{2}}$, and thus v^{v+1} . Thus, the particle evolution equations, (5.1) and (5.2), are solved implicitly using Picard iteration. The particle updates are coupled with the electromagnetic field updates using the Darwin model:

$$\epsilon_0 \frac{E_{x,\ell+\frac{1}{2}}^{n+1} - E_{x,\ell+\frac{1}{2}}^n}{\Delta t} + \sum_s \bar{j}_{s,x,\ell+\frac{1}{2}}^{n+\frac{1}{2}} - \left\langle \bar{j}_x^{n+\frac{1}{2}} \right\rangle = 0, \quad (5.3)$$

$$\frac{1}{\mu_0} \frac{A_{\perp,\ell-1}^{n+\frac{1}{2}} - 2A_{\perp,\ell}^{n+\frac{1}{2}} + A_{\perp,\ell+1}^{n+\frac{1}{2}}}{\Delta x^2} + \sum_s \bar{j}_{s,\perp,\ell}^{n+\frac{1}{2}} - \left\langle \bar{j}_\perp^{n+\frac{1}{2}} \right\rangle = 0, \quad (5.4)$$

where the current components $\bar{j}_{s,i,l}$ are orbit averaged over the substeps for each species, s . Here,

$$\bar{j}_{x,\ell+\frac{1}{2}}^{n+\frac{1}{2}} = \frac{1}{\Delta t \Delta x} \sum_p \sum_v q_p v_{p,x}^{v+\frac{1}{2}} S_m \left(x_p^{v+\frac{1}{2}} - x_{\ell+\frac{1}{2}} \right) \Delta \tau^v, \quad (5.5)$$

$$\bar{j}_{\perp,\ell}^{n+\frac{1}{2}} = \frac{1}{\Delta t \Delta x} \sum_p \sum_v q_p v_{p,\perp}^{v+\frac{1}{2}} S_l \left(x_p^{v+\frac{1}{2}} - x_\ell \right) \Delta \tau^v, \quad (5.6)$$

where S_m and S_l are B-spline shape functions used for consistency with the field-to-particle interpolation to achieve energy conservation, $\langle \bar{j}_i \rangle = \sum_{s,\ell} \bar{j}_{s,i,\ell} / N_x$ is the

spatial average of the net current density (i.e., adding both ion and electron current densities) and is necessary in periodic geometries to enforce periodicity of the fields (Chen, Chacón & Barnes 2011; Chen & Chacón, 2014), and N_x is the number of cells in the x direction.

5.2. Fluid model

The 10-moment plasma model solves the coupled set of fluid equations, which are written in one dimension using conservative variables:

$$\frac{\partial \mathbf{U}}{\partial t} + \frac{\partial \mathbf{F}}{\partial x} = \mathbf{S}, \quad (5.7)$$

where the vector of conservative variables $\mathbf{U} = \{\rho, \rho u_i, \rho u_i u_j + p_{ij}\} = \{\rho, \Gamma_i, S_{ij}\}$, the vector of conservative fluxes $\mathbf{F} = \{\rho u_x, \rho u_i u_x + p_{ix}, \rho u_i u_j u_x + u_i p_{jx} + u_j p_{xi} + u_x p_{ij}\}$ and the vector of conservative sources $\mathbf{S} = \{0, \rho E_i + \epsilon_{ijk} \rho u_j B_k, \rho u_i E_j + \rho u_j E_i + \epsilon_{ikl} (p_{jk} + \rho u_j u_k) B_l + \epsilon_{jkl} (p_{ik} + \rho u_i u_k) B_l\}$. Note that this conservative form of the equations is consistent with the primitive form which was used in the derivation of the dispersion relations in §2. The fluid equation is coupled with the Darwin equations, given in (2.23) and (2.24).

5.2.1. Numerical scheme

For the numerical solver, we employ a finite volume approach, in which the state variables are defined at the cell centres (Kuldinow *et al.* 2024a,b; Sahu, Mansour & Hara 2020). The fluid equations in one dimension are discretised using a Crank–Nicolson scheme:

$$\frac{\mathbf{U}_\ell^{n+1} - \mathbf{U}_\ell^n}{\Delta t} + \frac{\mathbf{F}_{\ell+\frac{1}{2}}^{n+\frac{1}{2}} - \mathbf{F}_{\ell-\frac{1}{2}}^{n+\frac{1}{2}}}{\Delta x} = \mathbf{S}_\ell^{n+\frac{1}{2}}, \quad (5.8)$$

while the Darwin equations are similarly discretised:

$$\epsilon_0 \frac{E_{x,\ell}^{n+1} - E_{x,\ell}^n}{\Delta t} + \sum_s j_{s,x,\ell}^{n+\frac{1}{2}} - \left\langle j_x^{n+\frac{1}{2}} \right\rangle = 0, \quad (5.9)$$

$$\frac{1}{\mu_0} \frac{A_{\perp,\ell-1}^{n+\frac{1}{2}} - 2A_{\perp,\ell}^{n+\frac{1}{2}} + A_{\perp,\ell+1}^{n+\frac{1}{2}}}{\Delta x^2} + \sum_s j_{s,\perp,\ell}^{n+\frac{1}{2}} - \left\langle j_\perp^{n+\frac{1}{2}} \right\rangle = 0, \quad (5.10)$$

where ℓ is the cell index and $\ell + \frac{1}{2}$ are cell interface positions, the superscript n denotes the time step, $j_{s,i} = q_s \Gamma_{s,i} / m_s$ and $\langle j_i \rangle = \sum_{s,\ell} j_{s,i,\ell} / N_x$. All quantities are defined at cell centres; interfacial values obtained using the monotonic upwinding scheme for conservation laws (MUSCL) with the van Leer harmonic limiter (van Leer 1979) are used to calculate the flux quantities.

Equations (5.8)–(5.10) can be written in the form

$$\mathcal{F}(\mathcal{M}^{n+1}, E_x^{n+1}, A_\perp^{n+1}) = \mathcal{F}(\mathbf{V}^{n+1}) = \mathbf{R} \Rightarrow 0, \quad (5.11)$$

where $\mathcal{M} = \{\rho, \Gamma_i, S_{ij}\}$ is the vector of fluid moments at all grid points and all quantities at time $t = t^n$ are assumed to be known for the nonlinear function \mathcal{F} , and \mathbf{R} is the residual which we want to vanish. The root of (5.11) is solved by a preconditioned Jacobian-free Newton Krylov iteration (Kelley 1995; Knoll & Keyes

2004). Given an initial guess for the solution at iteration κ , $\mathbf{V}^{n+1,(\kappa)}$, we can calculate the residual and update the solution vector as

$$\mathbf{V}^{n+1,(\kappa+1)} = \mathbf{V}^{n+1,(\kappa)} + \delta \mathbf{V}^{(\kappa)}, \quad (5.12)$$

where the update to the solution vector satisfies

$$\left[\frac{\partial \mathcal{F}}{\partial \mathbf{V}} \right]^{(\kappa)} \delta \mathbf{V}^{(\kappa)} = -\mathbf{R}^{(\kappa)}. \quad (5.13)$$

The inversion of the Jacobian matrix is handled through the preconditioned generalised minimum residual method (GMRES), and the Jacobian-vector product is estimated by a finite difference:

$$\left[\frac{\partial \mathcal{F}}{\partial \mathbf{V}} \right]^{(\kappa)} \delta \mathbf{V}^{(\kappa)} \simeq \frac{1}{\epsilon} \left[\mathcal{F}(\mathbf{V}^{(\kappa)} + \epsilon \delta \mathbf{V}^{(\kappa)}) - \mathcal{F}(\mathbf{V}^{(\kappa)}) \right] \quad (5.14)$$

for a small value of $\epsilon \simeq 10^{-8}$. The iteration (κ) is performed until convergence, determined by the magnitude of the residual $|\mathbf{R}| < \text{tol} = 10^{-8}$.

5.2.2. GMRES preconditioner

The GMRES preconditioner modifies (5.13) as

$$M^{-1} \left(\left[\frac{\partial \mathcal{F}}{\partial \mathbf{V}} \right]^{(\kappa)} \delta \mathbf{V}^{(\kappa)} \right) = M^{-1} (-\mathbf{R}^{(\kappa)}), \quad (5.15)$$

where M^{-1} is a function that is an approximate inverse of $\frac{\partial \mathcal{F}}{\partial \mathbf{V}}$, i.e. $M^{-1}(\mathbf{X}) \simeq \left(\frac{\partial \mathcal{F}}{\partial \mathbf{V}} \right)^{-1} \mathbf{X}$, allowing for faster convergence of the GMRES method. The function M^{-1} is determined by solving a simplified form of (5.13) and (5.14). To simplify and make the equations analytically invertible, we neglect the fluxes, \mathbf{F} , in (5.8) and neglect the effect of magnetic field coupling on the transverse momenta. Specifically, writing out the components of the simplified Newton step, we find

$$-R_{\rho, \ell} = \frac{\delta \rho_{\ell}}{\Delta t}, \quad (5.16)$$

$$\begin{aligned} -R_{\Gamma_{x, \ell}} = & \frac{\delta \Gamma_{x, \ell}}{\Delta t} - \frac{q}{2m} \left(\delta \rho_{\ell} E_{x, \ell}^{n+\frac{1}{2}} + \rho_{\ell}^{n+\frac{1}{2}} \delta E_{x, \ell} \right. \\ & \left. + \delta \Gamma_{y, \ell} B_{z, \ell}^{n+\frac{1}{2}} - \delta \Gamma_{z, \ell} B_{y, \ell}^{n+\frac{1}{2}} + \Gamma_{y, \ell}^{n+\frac{1}{2}} \delta B_{z, \ell} - \Gamma_{z, \ell}^{n+\frac{1}{2}} \delta B_{y, \ell} \right), \end{aligned} \quad (5.17)$$

$$-R_{\Gamma_{\perp, \ell}} = \frac{\delta \Gamma_{\perp, \ell}}{\Delta t} - \frac{q}{2m} \left(\delta \rho_{\ell} E_{\perp, \ell}^{n+\frac{1}{2}} + \rho_{\ell}^{n+\frac{1}{2}} \delta E_{\perp, \ell} \right), \quad (5.18)$$

$$\begin{aligned} -R_{S_{ij, \ell}} = & \frac{\delta S_{ij, \ell}}{\Delta t} - \frac{q}{2m} \left[\delta \Gamma_{i, \ell} E_{j, \ell}^{n+\frac{1}{2}} + \Gamma_{i, \ell}^{n+\frac{1}{2}} \delta E_{j, \ell} + \delta \Gamma_{j, \ell} E_{i, \ell}^{n+\frac{1}{2}} + \Gamma_{j, \ell}^{n+\frac{1}{2}} \delta E_{i, \ell} \right. \\ & \left. + \epsilon_{ikl} \left(\delta S_{jk, \ell} B_{l, \ell}^{n+\frac{1}{2}} - \delta S_{jk, \ell} B_{l, \ell}^{n+\frac{1}{2}} \right) + \epsilon_{jkl} \left(S_{ik, \ell}^{n+\frac{1}{2}} \delta B_{l, \ell} - S_{jk, \ell}^{n+\frac{1}{2}} \delta B_{l, \ell} \right) \right], \end{aligned} \quad (5.19)$$

$$-R_{E_x, \ell} = \epsilon_0 \frac{\delta E_{x, \ell}}{\Delta t} + \sum_s \frac{q_s \Gamma_{x, \ell}}{m_s} - \langle j_x \rangle, \quad (5.20)$$

$$-R_{A_{\perp, \ell}} = \frac{1}{\mu_0} \frac{\delta A_{\perp, \ell-1} - 2\delta A_{\perp, \ell} + \delta A_{\perp, \ell+1}}{\Delta x^2} + \sum_s \frac{q_s \Gamma_{\perp, \ell}}{m_s} - \langle j_{\perp} \rangle, \quad (5.21)$$

where $R_{Q, \ell}$ is the residual of the equation for quantity Q , and δQ are the components of $\delta \mathbf{V}$. In addition, the field quantities are updated as

$$\delta E_{\perp, \ell} = -\frac{\delta A_{\perp, \ell}}{\Delta t}, \quad (5.22)$$

$$\delta B_{i, \ell} = \epsilon_{ixk} \frac{\delta A_{k, \ell+1} - \delta A_{k, \ell-1}}{2\Delta x}. \quad (5.23)$$

Equations (5.18), (5.21) and (5.22) form a closed set, equivalent to a tridiagonal matrix-vector product, through which the preconditioner updates δA_{\perp} can be obtained and thus, δE_{\perp} , $\delta \Gamma_{\perp}$ and δB_i . Once those updates are known, (5.16), (5.17) and (5.20) are closed, and can be solved to obtain $\delta \rho$, $\delta \Gamma_x$ and δE_x . Finally, the previously determined quantities can be substituted into (5.19) to solve for δS_{ij} . This approximate inversion provides an approximate solution to (5.13), which is used as a preconditioner to the GMRES solution of the nonlinear Newton step, (5.15).

6. Numerical results

In this section, we present numerical results using 10-moment fluid and kinetic models, and compare to the theory presented above.

6.1. Initialisation

The set-up is an electron Weibel instability; all presented quantities are normalised as described in (3.1); we drop the tilde on all variables for the remainder of this section. We assume a periodic domain of length $L_x = 32$ (i.e. the domain wavenumber is $k_L = 2\pi/L_x \approx 0.196$) with $N_x = 128$ uniformly spaced cells, using the normalised units defined above. The kinetic simulations employ 2000 particles per cell and both models employ a time step of $\Delta t = 1$ (recall that time is normalised with $\omega_{e,p}^{-1}$). The initial electron distribution function is assumed to be a shifted bi-Maxwellian distribution:

$$f_e(x, v_i; t=0) = \frac{1}{\sqrt{2\pi} v_{e, \text{th}, \parallel} v_{e, \text{th}, \perp}^2} \exp \left[\frac{v_x^2}{2v_{e, \text{th}, \parallel}^2} + \frac{[v_y - u_{e,y}(x)]^2 + v_z^2}{2v_{e, \text{th}, \perp}^2} \right], \quad (6.1)$$

where $v_{e, \text{th}, i} = \sqrt{T_{e,i}}$ is the thermal velocity in the i direction and $u_{e,y}(x) = \delta \cos(k_L x)$ is a small initial transverse velocity perturbation, where $\delta = 1 \times 10^{-5}$ and $k_L = 2\pi/L_x$. We consider two test cases where $T_{\perp}/T_{\parallel} = 2.56$ and $T_{\perp}/T_{\parallel} = 25.6$. For both test cases, $T_{\parallel} = T_x = 6.25 \times 10^{-4}$. As shown in figure 1, for $T_{\perp}/T_{\parallel} = 2.56$, $\gamma_K = 4 \times 10^{-3}$ and $\gamma_{10M} = 6 \times 10^{-3}$ ($|\xi| \sim 0.6$), approximately a 50 % discrepancy between the kinetic and 10 M dispersion relations. However, for $T_{\perp}/T_{\parallel} = 25.6$, $\gamma_K = 2.30 \times 10^{-2}$ and $\gamma_{10M} = 2.38 \times 10^{-2}$ ($|\xi| \sim 3.3$), which results in only an approximately 3 % discrepancy, despite the moderate size of ξ .

In both cases, the initial conditions seed the fundamental wavenumber ($m=1$), determined by the domain size, which is not the wavenumber of maximum growth,

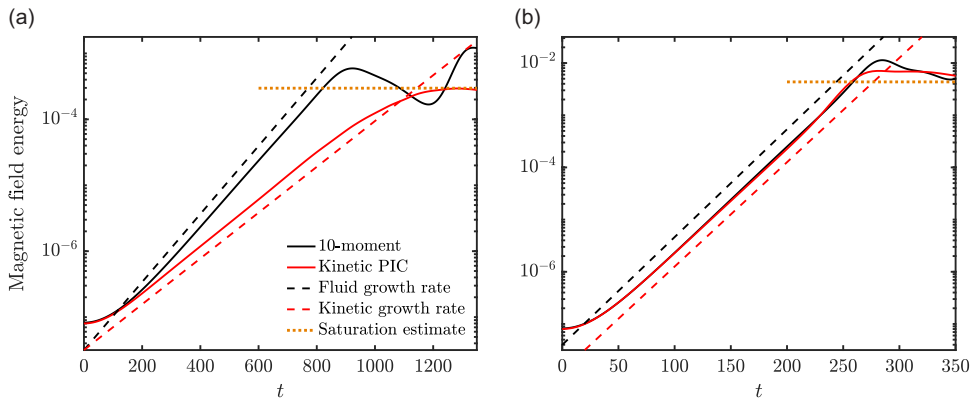


FIGURE 6. Temporal variation of magnetic field energy obtained from kinetic and fluid models. Comparisons are made to linear growth rate predictions, (2.2) and (2.27), and estimates of saturation field strength, (4.2), for (a) $T_{\perp}/T_{\parallel} = 2.56$ and (b) $T_{\perp}/T_{\parallel} = 25.6$.

k_{\max} , predicted by (3.4). For $T_{\perp}/T_{\parallel} = 2.56$, the growth rate is maximum at $k_{\max} = 0.775$, which is 3.9 times larger than k_L and the growth rate evaluated for k_L is 3.7 times smaller than the maximum growth rate. Additionally, for $T_{\perp}/T_{\parallel} = 25.6$, the growth rate is maximum at $k_{\max} = 2.01$, which is 10.3 times larger than k_L , resulting in a growth rate 4.3 times smaller than γ_{\max} . The initial conditions are kept ‘quiet’, i.e. noise-less, so that the fundamental k_L remains dominant through saturation. It is to be noted that in simulations with multimode or noisy initial conditions, the wavenumber of maximum growth, as predicted by the linear theory, is dominant.

The kinetic simulations each took approximately 4.5 hours, while the fluid simulations each took approximately 0.5 hours, using a single processor. It is however noted that the comparison of computational cost is highly dependent on the number of particles per cell in the kinetic simulation, and likewise, how important finite particle noise is to the system dynamics.

6.2. Comparison of results to linear and saturation theory

Figure 6 shows the total magnetic field energy, $\int_{\Omega_x} \frac{1}{2\mu_0} |B|^2 dx = \frac{\Delta x}{2\mu_0} \sum_{\ell} |B_{\ell}|^2$, as a function of time for the two T_{\perp}/T_{\parallel} cases.

In figure 6(a), we find good agreement between the simulation results and the linear growth rates obtained from both kinetic and fluid theories for $T_{\perp}/T_{\parallel} = 2.56$. It is to be noted that both computational models use the Darwin equations, thus neglecting the displacement current. For the non-relativistic set-ups ($c \gg \omega/k$) presented in this work, the discrepancy between the theoretical Maxwell and Darwin growth rates is less than 1 %, and does not drastically affect the saturation properties. We also find that, despite the different growth rates, the results obtained from the kinetic (PIC) and 10-moment fluid models saturate at approximately the same magnetic field energy, consistent with the field strength predicted by the saturation theory, as shown in (4.2).

Figure 6(b) shows good agreement between the simulation results and theory for the higher anisotropy case, i.e. $T_{\perp}/T_{\parallel} = 25.6$. The difference between the two predicted growth rates obtained from PIC and 10-moment dispersion relations agree

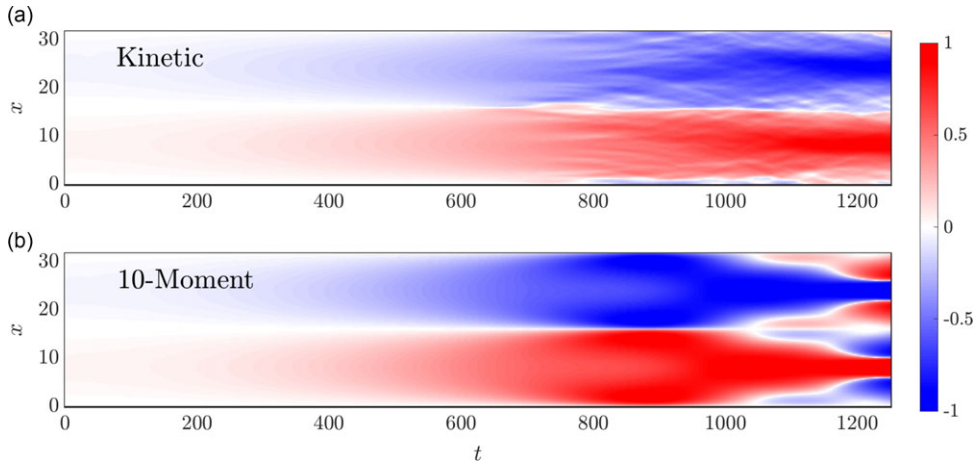


FIGURE 7. Symmetric logarithm of the magnetic field profile (6.2) for $T_{\perp}/T_{\parallel} = 2.56$: (a) kinetic simulation and (b) 10-moment fluid simulation.

to within 2.5 %, and again the results from both models saturate at nearly the same field strength, similar to that predicted by theory.

6.3. Comparison of magnetic field profiles

To provide a qualitative comparison of the fluid and kinetic results outside of the global metric of total magnetic field energy, we present the contour plots of the magnetic field in space and time. However, the magnetic field spans many scales due to the linear exponential growth phase and admits positive and negative values. Thus, for visualisation purposes, we will plot the symmetric logarithm of the magnetic field:

$$\text{symlog}[B(x), C] = \text{sgn}[B(x)] \log_{10}[1 + C|B(x)|]. \quad (6.2)$$

Unlike the common logarithm, the symmetric logarithm is continuous at zero but has the same asymptotic behaviour. For the remainder of this study, we will employ $C = 10^3$. This comes at the cost of losing information at scales smaller than 10^{-3} , for this choice of the constant. However, since we will be directing our attention towards the saturation properties of the magnetic field, this will not affect our discussion. Note that for $|B| \gg 10^{-3}$, $\text{symlog}[B(x), 10^3] \simeq \text{sgn}[B(x)] [3 + \log_{10}|B(x)|]$.

6.3.1. Low temperature ratio: $T_{\perp}/T_{\parallel} = 2.56$

Figure 7 shows $\text{symlog}[B(x), 10^3]$ for the initial temperature ratio $T_{\perp}/T_{\parallel} = 2.56$. Recall that for this lower temperature ratio, the growth rates of the kinetic and fluid descriptions of the Weibel instability differ by approximately 50 %, as shown in figure 6(a). The kinetic result, shown in figure 7(a), does not reach the peak magnetic field until $t \simeq 1250$, while the 10-moment result in figure 7(b) saturates early at approximately $t \simeq 800$. This is because the growth rates are estimated as $\gamma_K = 4 \times 10^{-3}$ and $\gamma_{10M} = 6 \times 10^{-3}$ for kinetic and 10-moment dispersion relations, respectively. We note that the kinetic simulation, due to wave mixing and non-thermal particles, generates high- k_x waves that look like ripples in the contour plots. These high- k_x structures born from individual particle dynamics eventually

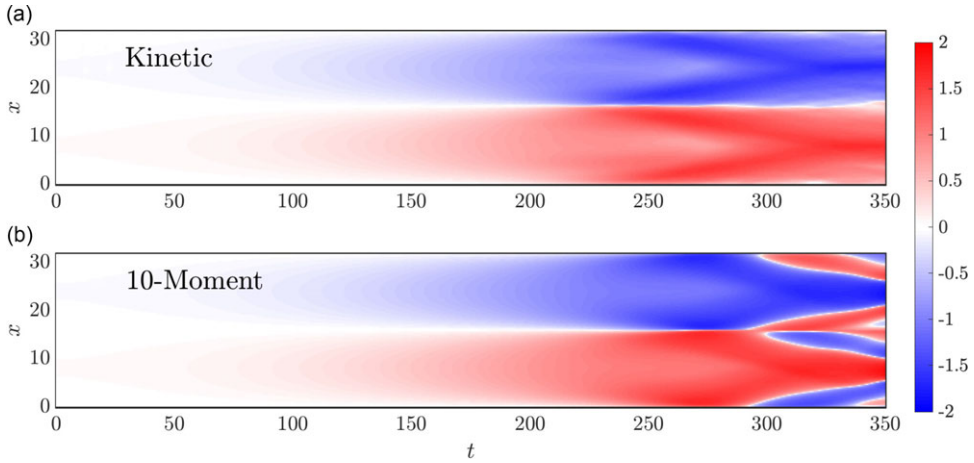


FIGURE 8. Symmetric logarithm of the magnetic field profile (6.2) for $T_{\perp}/T_{\parallel} = 25.6$: (a) kinetic simulation and (b) 10-moment simulation.

come to dominate the dynamics at saturation. In contrast, the 10-moment simulations capture neither the non-thermal particles nor significant deviations from Maxwellian; near saturation, the fluid model harmonics of the initial $m = 1$ mode also saturate and we observe less structured behaviour. Despite such a difference, the linear growth and nonlinear saturation is captured using the 10-moment fluid model.

6.3.2. High temperature ratio: $T_{\perp}/T_{\parallel} = 25.6$

Figure 8 shows $\text{symlog}[B(x), 10^3]$ for the initial temperature ratio $T_{\perp}/T_{\parallel} = 25.6$. Recall that for this higher temperature ratio, the growth rates of the kinetic and fluid descriptions of the Weibel instability agree well, as shown in figures 1 and 3. Furthermore, we can see that the profiles of the kinetic and fluid models at saturation ($t \simeq 275$) in figure 8 show approximately $m = 3$ modes ($k_x = 3k_{x,0}$, where $k_{x,0} = 2\pi/L_x$) before both models predict that higher k_x modes also saturate, leading to fine structure in the magnetic field profiles.

As with the lower temperature case, in figure 7, we note many small-amplitude, high- k_x ripples in the kinetic simulation, which grow to share nearly the same magnetic field energy as the fundamental mode at saturation. However, the fluid simulation is more ordered in the sense that after saturation, we observe a large-amplitude $m = 3$ mode near $t = 310$, then an $m = 5$ mode near $t = 350$, rather than the spectrum visible in the kinetic simulation. Again, this is most likely due to there being no damping mechanism in the fluid simulation (e.g. phase mixing), while the kinetic simulation necessarily exhibits particle-wave resonance and non-thermal diffusion. However, despite the fact that we are not capturing these inherently kinetic effects, it is remarkable that the 10-moment fluid model can accurately capture the linear growth and saturation level.

7. Conclusion

In this work, we have re-derived the dispersion relation for the Weibel instabilities from kinetic and multiple fluid frameworks which include full pressure tensor

dynamics (i.e. 10-moment fluid dispersion relation). We have quantified the error between the kinetic and fluid estimates for Weibel growth rates as a function of the perpendicular–parallel temperature ratio. In addition, we present an estimate of the saturation magnetic field derived from the 10-moment fluid theory and compare the 10-moment numerical simulations to the above. We find that the simulations are in excellent agreement with both linear and saturation theories, and thus consider the 10-moment fluid model to be verified against the theories presented above.

This work demonstrates the ability of the 10-moment fluid model that retains full pressure-tensor dynamics to accurately resolve the Weibel instability. In particular, the fluid and kinetic theories converge for the electron Weibel instability in the high perpendicular–parallel temperature ratio regime. In the low-temperature-ratio regime, although there is a discrepancy between the fluid theory the kinetic theory, the 10-moment fluid model is shown to capture approximately the correct saturation field strength.

Higher order moment models, e.g. the 13-moment model which directly evolves the heat flux, can capture the distribution function more accurately and thus retains more kinetic dynamics. Such models may be able to attain even better agreement with the kinetic results. Future work will investigate the Weibel instability in multiple spatial dimensions, its connection to the current filamentation instability, and the applicability of the 10-moment and other higher-order fluid moment models to capture magnetic field growth and saturation in astrophysical and laser-produced plasmas.

Acknowledgements

Editor Luís O. Silva thanks the referees for their advice in evaluating this article.

Funding

This work was supported by the U.S. Department of Energy National Nuclear Security Administration Stewardship Science Graduate Fellowship under cooperative agreement DE-NA0003960.

Declaration of interest

The authors report no conflict of interest.

Author contributions

D.A.K. derived the theory, made the numerical model and code, and visualised the results; K.H. contributed to data analysis and administered the project; all contributed to discussions during the research and to the writing and editing of the manuscript.

Data availability

The data that support the findings of this study are available from the corresponding author upon reasonable request.

Appendix A. Derivation of the MHD dispersion relation

To derive the Weibel dispersion relation in the MHD framework, we begin with MHD momentum equation, (2.32), the generalised Ohm's law, (2.35), Ampère's

law, (2.34):

$$\bar{\rho} \frac{\partial U_i}{\partial t} + U_j \frac{\partial U_i}{\partial x_j} = \epsilon_{ijk} j_j B_k - \frac{\partial p_{e,ij}}{\partial x_j}, \quad (\text{A.1})$$

$$\frac{\partial B_i}{\partial t} = \epsilon_{ijk} \frac{\partial}{\partial x_j} \left(\epsilon_{klm} U_l B_m + \frac{1}{e\bar{n}} \frac{\partial p_{e,kl}}{\partial x_l} - \frac{m_e}{\bar{n}e^2} \frac{\partial j_k}{\partial t} \right), \quad (\text{A.2})$$

$$\epsilon_{ijk} \frac{\partial B_k}{\partial x_j} = \mu_0 j_i. \quad (\text{A.3})$$

Then, considering only U_y , j_y , B_z and k_x , and taking linear perturbations around a stationary isotropic plasma, we obtain

$$-i\omega m_i \bar{n} U'_y = -ik_x p'_{e,xy} \Rightarrow U'_y = \frac{k_x}{\omega m_i \bar{n}} p'_{e,xy}, \quad (\text{A.4})$$

$$-i\omega B'_z = ik_x \left(\frac{1}{e\bar{n}} ik_x p'_{e,xy} + i \frac{\omega m_e}{\bar{n}e^2} j'_y \right) = -\frac{k_x^2}{e} \frac{p'_{e,xy}}{\bar{n}} - \frac{k_x \omega m_e}{\bar{n}e^2} j'_y, \quad (\text{A.5})$$

$$-ik_x B'_z = \mu_0 j'_y \Rightarrow j'_y = -\frac{ik_x}{\mu_0} B'_z. \quad (\text{A.6})$$

The term corresponding to the unsteady term in Ohm's law has been underlined to keep track of how it influences the equations. Now, we combine these results with the linearised fluid equation for $p'_{e,xy}$, (2.16):

$$-i\omega p'_{e,xy} + ik_x p_{e,\parallel} u'_{e,y} = -\frac{eB'_z}{m_e} (p_{e,\perp} - p_{e,\parallel}). \quad (\text{A.7})$$

However, since the MHD approximation does not solve for u_s directly, we must solve for it in terms of U and j . Assuming that $m_i \gg m_e$, (2.29) reduces to $u_{i,k} = U_k$ and thus,

$$u_e = u_i - \frac{e\bar{n}u_i - e\bar{n}u_e}{e\bar{n}} = U - \frac{j}{e\bar{n}}. \quad (\text{A.8})$$

Plugging (A.8) into (A.7), we find that

$$p'_{e,xy} = \frac{eB'_z}{im_e\omega} p_{e,\parallel} \left(\frac{T_{e,\perp}}{T_{e,\parallel}} - 1 \right) + p_{e,\parallel} \frac{k_x}{\omega} \left(U'_y - \frac{j'_y}{e\bar{n}} \right). \quad (\text{A.9})$$

Likewise, plugging (A.4), (A.6) into (A.9), we have that

$$p'_{e,xy} = \frac{eB'_z}{im_e\omega} p_{e,\parallel} \left(\frac{T_{e,\perp}}{T_{e,\parallel}} - 1 \right) + p_{e,\parallel} \frac{k_x}{\omega} \left(\frac{k_x}{\omega m_i \bar{n}} p'_{e,xy} + \frac{ik_x B'_z}{\mu_0 e \bar{n}} \right). \quad (\text{A.10})$$

Isolating $p_{e,xy}$, we find

$$p'_{e,xy} = \left(1 - \frac{k_x^2 p_{e,\parallel}}{\omega^2 m_i \bar{n}} \right)^{-1} p_{e,\parallel} \frac{eB'_z}{im_e\omega} \left(\frac{T_{e,\perp}}{T_{e,\parallel}} - 1 - \frac{k_x^2 c^2}{\omega_{e,p}^2} \right). \quad (\text{A.11})$$

Then, putting (A.6) and (A.11) into (A.5), we obtain

$$-i\omega B'_z = -\frac{k_x^2}{e\bar{n}} \left(1 - \frac{k_x^2 p_{e,\parallel}}{\omega^2 m_i \bar{n}}\right)^{-1} p_{e,\parallel} \frac{eB'_z}{im_e \omega} \left(\frac{T_{e,\perp}}{T_{e,\parallel}} - 1 - \frac{k_x^2 c^2}{\omega_{e,p}^2}\right) + \frac{k_x^2 c^2}{\omega_{e,p}^2} i\omega B'_z. \quad (\text{A.12})$$

Then, dividing through by $i\omega B'_z$ and simplifying yields that

$$-1 = -\left(1 - \frac{k_x^2 p_{e,\parallel}}{\omega^2 m_i \bar{n}}\right)^{-1} \frac{k_x^2 p_{e,\parallel}}{\omega^2 m_e \bar{n}} \left(\frac{k_x^2 c^2}{\omega_{e,p}^2} - \frac{T_{e,\perp}}{T_{e,\parallel}} + 1\right) + \frac{k_x^2 c^2}{\omega_{e,p}^2}. \quad (\text{A.13})$$

Recalling that $\xi^2 = \omega^2 m_e \bar{n} / (2k_x^2 p_{e,\parallel})$ and $m_e \ll m_i$, we can write

$$-1 = \frac{1}{2\xi^2} \left(\frac{k_x^2 c^2}{\omega_{e,p}^2} - \frac{T_{e,\perp}}{T_{e,\parallel}} + 1\right) + \frac{k_x^2 c^2}{\omega_{e,p}^2}. \quad (\text{A.14})$$

Now, we can rewrite this equation as

$$-\frac{k_x^2 c^2}{\omega_{e,p}^2} \left(1 - \frac{1}{2\xi^2}\right) - \left(1 - \frac{1}{2\xi^2}\right) - \frac{1}{\xi^2} \frac{T_{e,\perp}}{2T_{e,\parallel}} = 0. \quad (\text{A.15})$$

Multiplying through by $\omega_{e,p}^2 / [\omega^2 (1 - 1/2\xi^2)]$ to isolate $(k_x c / \omega)^2$ yields the desired result:

$$D_{10\text{MHD}}(k_x, \omega) = -\frac{k_x^2 c^2}{\omega^2} - \frac{\omega_p^2}{\omega^2} \left(\frac{2\xi^2 - 1}{2\xi^2 - 1} + \frac{T_{\perp}}{2T_{\parallel}} \frac{1}{\xi^2 - 1/2}\right) = 0, \quad (\text{A.16})$$

where we have dropped the electron species subscript. Recalling that the green terms are associated with the unsteady term in Ohm's law, we can find that

$$D_{10\text{MHD}}(k_x, \omega) = \begin{cases} -\frac{k_x^2 c^2}{\omega^2} - \frac{\omega_p^2}{\omega^2} \left(1 + \frac{T_{\perp}}{2T_{\parallel}} \frac{1}{\xi^2 - 1/2}\right) = 0 & \text{with unsteady Ohm's law,} \\ -\frac{k_x^2 c^2}{\omega^2} - \frac{\omega_p^2}{\omega^2} \left(1 - \frac{T_{\perp}}{T_{\parallel}} - 2\xi^2\right) = 0 & \text{without unsteady Ohm's law.} \end{cases} \quad (\text{A.17})$$

Let us compare this to the (Darwin) kinetic dispersion relation for the electron Weibel instability:

$$D_K(k_x, \omega) = -\frac{k_x^2 c^2}{\omega^2} - \frac{\omega_p^2}{\omega^2} \left[1 + \frac{T_{\perp}}{2T_{\parallel}} Z'(\xi)\right] = 0, \quad (\text{A.18})$$

and using the asymptotic expansions for $Z'(\xi)$,

$$D_K(k_x, \omega) \approx \begin{cases} -\frac{k_x^2 c^2}{\omega^2} - \frac{\omega_p^2}{\omega^2} \left(1 + \frac{T_{\perp}}{2T_{\parallel}} \frac{1}{\xi^2}\right) = 0 & \text{for } \xi \gg 1, \\ -\frac{k_x^2 c^2}{\omega^2} - \frac{\omega_p^2}{\omega^2} \left(1 - \frac{T_{\perp}}{T_{\parallel}} + 2\xi^2 \frac{T_{\perp}}{T_{\parallel}} - 2i \frac{T_{\perp}}{T_{\parallel}} \sqrt{\pi} \xi e^{-\xi^2}\right) = 0 & \text{for } \xi \ll 1. \end{cases} \quad (\text{A.19})$$

We note that only the MHD dispersion relation that includes the unsteady term in Ohm's law is asymptotically consistent with the large ξ limit of the kinetic dispersion relation. The MHD dispersion relation that does not include the unsteady term in Ohm's law is similar in form to the small ξ limit of the kinetic dispersion relation, but has the wrong coefficient on the second order term, and so is only consistent at $\xi = 0$ (cutoff condition), but will predict incorrect linear behaviour for all finite ξ .

REFERENCES

- BASU, B. 2002 Moment equation description of Weibel instability. *Phys. Plasmas* **9** (12), 5131–5134.
- BYCHENKOV, V.Y., SILIN, V.P. & TIKHONCHUK, V.T. 1989 Singular vortex flows in plasmas with anisotropic pressure. *Phys. Lett. A* **138** (3), 127–130.
- CAGAS, P., HAKIM, A., JUNO, J. & SRINIVASAN, B. 2017*a* Continuum kinetic and multi-fluid simulations of classical sheaths. *Phys. Plasmas* **24** (2), 022118.
- CAGAS, P., HAKIM, A., SCALES, W. & SRINIVASAN, B. 2017*b* Nonlinear saturation of the Weibel instability. *Phys. Plasmas* **24** (11), 112116.
- CALIFANO, F., PEGORARO, F. & BULANOV, S.V. 1997 Spatial structure and time evolution of the Weibel instability in collisionless inhomogeneous plasmas. *Phys. Rev. E* **56** (1), 963–969.
- CALIFANO, F., PEGORARO, F., BULANOV, S.V. & MANGENEY, A. 1998 Kinetic saturation of the Weibel instability in a collisionless plasma. *Phys. Rev. E* **57** (6), 7048–7059.
- CHANG, C.L., WONG, H.K. & WU, C.S. 1990 Electromagnetic instabilities attributed to a cross-field ion drift. *Phys. Rev. Lett.* **65** (9), 1104–1107.
- CHEN, G. & CHACÓN, L. 2014 An energy-and charge-conserving, nonlinearly implicit, electromagnetic 1D-3V Vlasov–Darwin particle-in-cell algorithm. *Comput. Phys. Commun.* **185** (10), 2391–2402.
- CHEN, G., CHACÓN, L. & BARNES, D.C. 2011 An energy-and charge-conserving, implicit, electrostatic particle-in-cell algorithm. *J. Comput. Phys.* **230** (18), 7018–7036.
- FIÚZA, F., FONSECA, R.A., TONGE, J., MORI, W.B. & SILVA, L.O. 2012 Weibel-instability-mediated collisionless shocks in the laboratory with ultraintense lasers. *Phys. Rev. Lett.* **108** (23), 235004.
- FRIED, B.D. & CONTE, S.D. 2015 *The Plasma Dispersion Function: the Hilbert Transform of the Gaussian*. Academic press.
- GAUTSCHI, W. 1970 Efficient computation of the complex error function. *SIAM J. Numer. Anal.* **7** (1), 187–198.
- GHIZZO, A., SARRAT, M. & DEL SARTO, D. 2017 Vlasov models for kinetic Weibel-type instabilities. *J. Plasma Phys.* **83** (1), 705830101.
- GRASSI, A., GRECH, M., AMIRANOFF, F., PEGORARO, F., MACCHI, A. & RICONDA, C. 2017 Electron Weibel instability in relativistic counterstreaming plasmas with flow-aligned external magnetic fields. *Phys. Rev. E* **95** (2), 023203.
- HAKIM, A.H. 2008 Extended MHD modelling with the ten-moment equations. *J. Fusion Energy* **27** (1-2), 36–43.
- HAMMETT, G.W. & PERKINS, F.W. 1990 Fluid moment models for Landau damping with application to the ion-temperature-gradient instability. *Phys. Rev. Lett.* **64** (25), 3019–3022.
- HUNTINGTON, C.M., *et al.* 2015 Observation of magnetic field generation via the Weibel instability in interpenetrating plasma flows. *Nat. Phys.* **11** (2), 173–176.
- JI-WEI, L. & WEN-BING, P. 2005 Effect of guiding magnetic field on Weibel instability. *Chin. Phys. Lett.* **22** (8), 1976.
- KAANG, H.H., RYU, C.-M. & YOON, P.H. 2009 Nonlinear saturation of relativistic Weibel instability driven by thermal anisotropy. *Phys. Plasmas* **16** (8), 082103.
- KELLEY, C.T. 1995 Iterative methods for linear and nonlinear equations. *Society for Industrial and Applied Mathematics*, Philadelphia.
- KNOLL, D.A. & KEYES, D.E. 2004 Jacobian-free Newton–Krylov methods: a survey of approaches and applications. *J. Comput. Phys.* **193** (2), 357–397.
- KRALL, N.A., TRIVELPIECE, A.W. & GROSS, R.A. 1973 Principles of plasma physics. *Am. J. Phys.* **41** (12), 1380–1381.

- KULDINOW, D.A., YAMASHITA, Y. & HARA, K. 2024a Ten-moment fluid model for low-temperature magnetized plasmas. *Phys. Plasmas* **31** (12), 123506.
- KULDINOW, D.A., YAMASHITA, Y., MANSOUR, A.R. & HARA, K. 2024b Ten-moment fluid model with heat flux closure for gasdynamic flows. *J. Comput. Phys.* **508**, 113030.
- LAISHRAM, M., YUN, G.S. & YOON, Y.D. 2024 Magnetogenesis via the canonical battery effect. *Phys. Rev. Res.* **6** (3), L032052.
- VAN LEER, B. 1979 Towards the ultimate conservative difference scheme. V. A second-order sequel to Godunov's method. *J. Comput. Phys.* **32** (1), 101–136.
- MITCHNER, M. & KRUGER, C.H.Jr. 1973 *Partially Ionized Gases*. John Wiley and Sons, Inc.
- MONDAL, S., *et al.* 2012 Direct observation of turbulent magnetic fields in hot, dense laser produced plasmas. *Proc. Natl Acad. Sci. USA* **109** (21), 8011–8015.
- MORSE, R.L. & NIELSON, C.W. 1970 Numerical simulation of the Weibel instability in one and two dimensions. Los Alamos, NM (United States): Los Alamos National Lab.(LANL), Tech. Rep.
- NG, J., HAKIM, A., WANG, L. & BHATTACHARJEE, A. 2020 An improved ten-moment closure for reconnection and instabilities. *Phys. Plasmas* **27** (8), 082106.
- NIELSON, C.W. & LEWIS, H.R. 1976 Particle code models in the nonradiative limit. *Meth. Comput. Phys.* **16**, 367–388.
- NISHIKAWA, K.-I., HARDEE, P.E., HEDEDAL, C.B. & FISHMAN, G.J. 2006 Acceleration mechanics in relativistic shocks by the Weibel instability. *Astrophys. J.* **642** (2), 1267–1274.
- NISHIKAWA, K.-I., HARDEE, P., RICHARDSON, G., PREECE, R., SOL, H. & FISHMAN, G.J. 2003 Particle acceleration in relativistic jets due to Weibel instability. *Astrophys. J.* **595** (1), 555–563.
- OKADA, T. & OGAWA, K. 2007 Saturated magnetic fields of Weibel instabilities in ultraintense laser-plasma interactions. *Phys. Plasmas* **14** (7), 072702.
- PEGORARO, F., BULANOV, S.V., CALIFANO, F. & LONTANO, M. 1996 Nonlinear development of the Weibel instability and magnetic field generation in collisionless plasmas. *Phys. Scripta* **T63**, 262–265.
- REN, C., TZOUFRAS, M., TSUNG, F.S., MORI, W.B., AMORINI, S., FONSECA, R.A., SILVA, L.O., ADAM, J.-C. & HERON, A. 2004 Global simulation for laser-driven MeV electrons in fast ignition. *Phys. Rev. Lett.* **93** (18), 185004.
- ROMANOV, D.V., BYCHENKOV, VYU, ROZMUS, W., CAPIACK, C.E. & FEDOSEJEVS, R. 2004 Self-organization of a plasma due to 3D evolution of the Weibel instability. *Phys. Rev. Lett.* **93** (21), 215004.
- RUYER, C., GREMILLET, L., DEBAYLE, A. & BONNAUD, G. 2015 Nonlinear dynamics of the ion Weibel-filamentation instability: an analytical model for the evolution of the plasma and spectral properties. *Phys. Plasmas* **22** (3), 032102.
- SAHU, R., MANSOUR, A.R. & HARA, K. 2020 Full fluid moment model for low temperature magnetized plasmas. *Phys. Plasmas* **27** (11), 113505.
- SARRAT, M., DEL SARTO, D. & GHIZZO, A. 2016 Fluid description of Weibel-type instabilities via full pressure tensor dynamics. *Europhys. Lett.* **115** (4), 45001.
- SARRAT, M., DEL SARTO, D. & GHIZZO, A. 2017 A pressure tensor description for the time-resonant Weibel instability. *J. Plasma Phys.* **83** (1), 705830103.
- SHARMA, P., HAMMETT, G.W., QUATAERT, E. & STONE, J.M. 2006 Shearing box simulations of the MRI in a collisionless plasma. *Astrophys. J.* **637** (2), 952–967.
- STOCKEM, A., DIECKMANN, M.E. & SCHLICKSEISER, R. 2008 Suppression of the filamentation instability by a flow-aligned magnetic field: testing the analytic threshold with PIC simulations. *Plasma Phys. Control. Fusion* **50** (2), 025002.
- STOCKEM, A., LERCHE, I. & SCHLICKSEISER, R. 2007 The relativistic filamentation instability in magnetized plasmas. *Astrophys. J.* **659** (1), 419–425.
- TATARAKIS, M., *et al.* 2003 Propagation instabilities of high-intensity laser-produced electron beams. *Phys. Rev. Lett.* **90** (17), 175001.
- WEIBEL, E.S. 1959 Spontaneously growing transverse waves in a plasma due to an anisotropic velocity distribution. *Phys. Rev. Lett.* **2** (3), 83–84.

- YOON, Y.D. & BELLAN, P.M. 2019 The electron canonical battery effect in magnetic reconnection: completion of the electron canonical vorticity framework. *Phys. Plasmas* **26** (10), 100702.
- ZAGHLOUL, M.R. & ALI, A.N. 2012 Algorithm 916: computing the Faddeyeva and Voigt functions. *ACM Trans. Math. Softw.* **38** (2), 1–22.
- ZHANG, C., *et al.* 2020 Measurements of the growth and saturation of electron Weibel instability in optical-field ionized plasmas. *Phys. Rev. Lett* **125** (25), 255001.